11-7-2016

Size and Site Dependence of the Catalytic Activity of Iridium Clusters towards Ethane Dehydrogenation

Yingbin Ge

Hao Jiang

Russell Kato

Prasuna Gummagatta

Size and Site Dependence of the Catalytic Activity of Iridium Clusters towards Ethane Dehydrogenation

Yingbin Ge*, Hao Jiang, Russell Kato, Prasuna Gummagatta

Department of Chemistry, Central Washington University, Ellensburg, WA 98926, United States

* Corresponding author. Tel.: +1 509 963 2817; Fax: +1 509 963 1050. E-mail address: yingbin@cwu.edu (Y. Ge).

Abstract

This research focuses on optimizing transition metal nanocatalyst immobilization and activity to enhance ethane dehydrogenation. Ethane dehydrogenation, catalyzed by thermally stable Ir_n (n = 8, 12, 18) atomic clusters that exhibit a cuboid structure, was studied using the B3LYP method with triple-ζ basis sets. Relativistic effects and dispersion corrections were included in the calculations. In the dehydrogenation reaction $Ir_n + C_2H_6 \rightarrow H{-}Ir_n{-}C_2H_5 \rightarrow (H)_2{-}Ir_n{-}C_2H_4$, the first H-elimination is the rate-limiting step, primarily because the reaction releases sufficient heat to facilitate the second H-elimination. The catalytic activity of the Ir clusters strongly depends on the Ir cluster size and the specific catalytic site. Cubic Ir_8 is the least reactive towards H-elimination in ethane: $Ir_8 + C_2H_6 \rightarrow H{-}Ir_8{-}C_2H_5$ has a large (65 kJ/mol) energy barrier, whereas Ir_{12} (3×2×2 cuboid) and Ir_{18} (3×3×2 cuboid) lower this energy barrier to 22 kJ/mol and 3 kJ/mol, respectively. The site dependence is as prominent as the size effect. For example, the energy barrier for the $Ir_{18} + C_2H_6 \rightarrow H{-}Ir_{18}{-}C_2H_5$ reaction is 3 kJ/mol, 48 kJ/mol, and 71 kJ/mol at the corner, edge, or face-center sites of the Ir_{18} cuboid, respectively. Energy release due to Ir cluster insertion into an ethane C–H bond facilitates hydrogen migration on the Ir cluster surface, and the second H-elimination of ethane. In an oxygen-rich environment, oxygen molecules may be absorbed on the Ir cluster surface. The oxygen atoms bonded to the Ir cluster surface may slightly increase the energy barrier for H-elimination in ethane. However, the adsorption of oxygen and its reaction with H atoms on the Ir cluster releases sufficient heat to yield an overall thermodynamically favored reaction: $Ir_n + C_2H_6 + ½\ O_2 \rightarrow Ir_n + C_2H_4 + H_2O$. These results will be useful towards reducing the energy cost of ethane dehydrogenation in industry.

1. Introduction

Ethane dehydrogenation is a multibillion-dollar process in the petroleum industry. Consequently, transition metal catalyst activity towards dehydrogenation of ethane and other light alkanes has been extensively studied both experimentally and theoretically.[1] Specifically, metal oxide surface-supported transition metal nanoclusters are particularly effective towards catalyzed alkane dehydrogenation.[2–7] Despite the extraordinary catalytic activity of these supported transition metal nanocatalysts, their migration on supporting surfaces often leads to undesired coalescence and catalyst deactivation.[8] Various methods have been used to prevent supported nanocatalyst deactivation, such as using surface defects to trap the nanocatalysts.[9] Instead of focusing on the anchoring ability of the supporting surface, we aim to design a catalytic system that prevents nanocatalyst migration by increasing nanocatalyst cluster size. By so doing, more chemical bonds can be formed between larger clusters and their supporting surface. Consequently, the surface-supported clusters must overcome a larger energy barrier to migrate. However, larger cluster sizes can be problematic because transition metal nanocatalysts often lose their catalytic activity at a sufficiently large cluster size. This research focuses on overcoming previous catalytic limitations by optimizing both nanocatalyst immobilization and activity.

This paper focuses on the catalytic activity of iridium clusters (Ir_8, Ir_{12}, and Ir_{18}) towards ethane dehydrogenation. Smaller Ir_4 and Ir_6 clusters that are supported on metal oxide surfaces exhibit extraordinary catalytic activity towards ethene hydrogenation and reversible ethane dehydrogenation.[2,3,5] However, such small Ir clusters tend to migrate on their supporting surface. For example, the energy barrier of Ir_3 migration on a MgO surface is only approximately 40 kJ/mol.[8] Larger Ir_8, Ir_{12}, and Ir_{18} clusters with a cubic or cuboid structure may have 4, 6, and 9 Ir

atoms forming chemical bonds to their supporting surface and thus are less likely to migrate than Ir_3. Our choice of these three cluster sizes (n = 8, 12, 18) was also motivated by their predicted thermodynamic favorability than similar sizes.[10,11] Chen et al. found that Ir_8 tends to adopt a very stable cubic structure at the CASSCF and CCSD(T) levels of theory.[11] Davis et al. found that the global minima of Ir_8, Ir_{12}, and Ir_{18} adopts a cubic or cuboid structure via PBE density functional theory (DFT) calculations.[10] The plot of energy second-order derivatives with respect to cluster sizes suggests that Ir clusters with an even number of atoms are more stable than those with an odd number of atoms; Ir_8, Ir_{12}, and Ir_{18} cubic/cuboid structures are particularly stable and thus 8, 12, and 18 may be considered "magic numbers" of Ir clusters.[10] These magic numbers are not unique to Ir nanoclusters: Ru_8 and Ru_{12} prefer to adopt a cubic or cuboid structure and are particularly stable in comparison with Ru clusters of similar sizes.[12] Because thermal stability may also hinder nanocatalyst deformation and activation, we studied catalysis of Ir_8, Ir_{12}, and Ir_{18} cuboid structures with respect to ethane dehydrogenation.

Ir_n (n = 8, 12, 18) cluster-catalyzed ethane dehydrogenation involves two steps: i) insertion of an Ir_n cluster into a C−H bond of ethane, $Ir_n + C_2H_6 \rightarrow H{-}Ir_n{-}C_2H_5$; and ii) the same Ir cluster breaks a second C−H bond, $H{-}Ir_n{-}C_2H_5 \rightarrow (H)_2{-}Ir_n{-}C_2H_4$. In an oxygen-rich environment, hydrogen atoms on the Ir cluster surface react with adsorbed oxygen to form water. Overall, when the endothermic $C_2H_6 \rightarrow C_2H_4 + H_2$ reaction ($\Delta H_R^o = 136.4$ kJ/mol)[13] is coupled with the reaction $H_2 + ½O_2 \rightarrow H_2O$ ($\Delta H_R^o = -285.8$ kJ/mol),[13] oxidative dehydrogenation of ethane, $C_2H_6 + ½O_2 \rightarrow C_2H_4 + H_2O$, becomes strongly exothermic: $\Delta H_R^o = -149.4$ kJ/mol at 298 K. Due to the strong thermodynamic favorability from hydrogen atom oxidation, Ir_n cluster-facilitated cleavage of two C–H bonds of ethane, $Ir_n + C_2H_6 \rightarrow H{-}Ir_n{-}C_2H_5 \rightarrow (H)_2{-}Ir_n{-}C_2H_4$, is

more likely the bottleneck of ethane oxidative dehydrogenation. Hence, these two H-eliminations steps are the focus of this computational study.

2. Computational Methods

The B3LYP DFT method[14–16] was used for all of the calculations. Chen et al. showed that B3LYP clearly outperforms PW91 and SVWN with respect to Ir cluster calculations.[11] The B3LYP method was also compared with several other DFT methods against the coupled-cluster benchmark calculations for small Ir compounds; B3LYP balanced accuracy and computational cost (see subsection 3.1). The D3 empirical dispersion formulated by Grimme with Becke–Johnson damping[17] (D3BJ) was included in all B3LYP calculations. In the geometry optimization and vibrational frequency calculations, polarized double-ζ basis sets were used: the LANL2DZ basis set and the LANL2 effective core potential (ECP),[18] augmented with f-type polarization functions,[19] were employed on the Ir atoms; and the 6-31G(d) basis sets were employed on the C, H, and O atoms.[20,21] To further improve the accuracy, single-point energies were calculated using polarized triple-ζ basis sets: the LANL2TZ(f) basis set[18,19,22] was employed on the Ir atoms; and the 6-311G(d,p) basis sets on the C, H, and O atoms.[23] The harmonic-oscillator rigid-rotor approximation was made in the vibrational frequency calculations. The scaling factor for the zero-point energy, enthalpy, and entropy calculations was set to be 1. Spin-orbit coupling was negligible for Ir_8 and larger clusters[11], and thus was not included in the calculations.

An extensive search for the lowest-energy-barrier reaction paths of $Ir_n + C_2H_6 \rightarrow H{-}Ir_n{-}C_2H_5 \rightarrow (H)_2{-}Ir_n{-}C_2H_4$ was conducted in various spin states. Intrinsic reaction coordinate (IRC) calculations were performed for every transition state (TS) to ensure that the TS structure connects the desired reactant and product. The Cartesian coordinates and vibrational frequencies of the transition state structures are included in the Supporting Information.

Coupled-cluster benchmark calculations were performed using GAMESS software;[24,25] DFT calculations were performed using the Gaussian 09 package.[26]

3. Results and Discussion

3.1 Computational method assessment

We first assessed numerous computational methods for accuracy and computational cost. We compared six widely used DFT methods, including the double-hybrid B2PLYP[27] with HF exchange and MP2-type correlation, the single-hybrid B3LYP[14–16] and PBE0[28] methods with HF exchange, and the pure BLYP,[15,29] PBE,[30] and SVWN[31–34] methods. The bond energies of IrH, IrC, IrO, and IrO_2 were calculated using the aforementioned DFT methods, and by using the benchmark CR-CC(2,3) method, in which CR-CC(2,3) stands for the left-eigenstate completely renormalized singles, doubles, and perturbative triples method.[35–38] The same basis sets as described in the Computational Methods section were used consistently in all of the DFT and CR-CC(2,3) calculations. Table 1 shows that the double-hybrid B2PLYP method clearly outperforms the hybrid B3LYP and PBE0 methods, and that the three pure DFT methods are the least accurate. However, calculation of the MP2-type correlation in B2PLYP becomes prohibitively computationally expensive for larger Ir clusters such as Ir_{18}. Therefore, practical considerations of limited computing resources dictated the choice of B3LYP. Chen and Dixon also recommend the B3LYP method for Ir cluster modeling.[11]

Table 1. Deviations and mean absolute deviation of the DFT calculated bond energy relative to the CR-CC(2,3) benchmark calculations. All values are in kJ/mol.

	B2PLYP	B3LYP	BLYP	PBE0	PBE	SVWN
^{3}IrH	3.1	−10.1	−3.5	−4.5	−27.4	−95.2
^{2}IrC	−9.2	34.2	−13.8	23.4	−73.4	−195.7
^{2}IrO	−2.5	23.6	−52.6	30.8	−62.2	−233.5
$^2IrO_2$	−13.5	26.1	−72.5	34.8	−126.9	−226.9
Mean Absolute Deviation	7.1	23.5	35.6	23.4	72.5	187.8

Inclusion of the D3BJ dispersion corrections was important, as illustrated in Figure 1 via

a comparison of the atomization energy per atom for Ir_n clusters, with the dispersion correction versus without the correction. The magnitude of the dispersion correction increases appreciably as the Ir cluster size increases from 2 to 18.

Our B3LYP–D3BJ calculations suggest that the Ir_8 global minimum has a multiplicity of 13, which is in agreement with Chen and Dixon's coupled-cluster calculations.[11] The multiplicity of the lowest-energy Ir_{12} cuboid is 11, which is different from the PBE prediction (M = 3).[10] For the Ir_{18} cuboid structure, we found three nearly degenerate electronic states (M = 3, 5, 7) with the lowest energies, which is in reasonable agreement with the PBE calculations (M = 7).[10] In summary, the B3LYP–D3BJ calculations agree with the previous CCSD(T) calculations and partially with the PBE calculations; our assessment of the DFT methods for small Ir molecules suggests that hybrid DFT methods (e.g., B3LYP) in general outperform the pure DFT methods (e.g., PBE). A similar study also found that hybrid DFT methods ourform pure methods for analogous platinum molecules.[39]

Because of the many nearly degenetate electronic states in Ir clusters, it is necessary to investigate the Ir cluster-catalyzed hydrogen elimination of ethane in various spin states, as described next.

3.2 First hydrogen elimination: $Ir_n + C_2H_6 \rightarrow H{-}Ir_n{-}C_2H_5$

The energy profiles of the $Ir_n + C_2H_6 \rightarrow H{-}Ir_n{-}C_2H_5$ reaction path were calculated in various spin states. For Ir_8, reaction paths in eight spin states (S = 0−7) were calculated; this ensured that at least one reaction path was calculated with its spin quantum number higher than that of the Ir_8 global minimum in the 13-et state with S = 6, in which the multiplicity (M) equals 2S + 1. Ir_8 clusters with S > 7 have much higher energy and thus were not investigated further. For Ir_{12} and Ir_{18}, reaction paths in seven different spin states (S = 0−6) were calculated; spin

states that are higher than S = 6 have much higher energies and thus were not investigated further.

Figure 2(a) illustrates the eight reaction paths of $Ir_8 + C_2H_6 \rightarrow H{-}Ir_8{-}C_2H_5$ in various spin states. Each of the eight reaction paths consists of four structures: i) separate Ir_8 and ethane reactants ($Ir_8 + C_2H_6$); ii) the reaction complex ($Ir_8{---}C_2H_6$), where the "---" symbol denotes the attractive interaction between the Ir cluster and ethane; iii) the TS in which the C–H bond is partially broken while the Ir–H and Ir–C bonds are partially formed; and iv) the product ($H{-}Ir_8{-}C_2H_5$). The total energy of separated $^{13}Ir_8$ global minimum and C_2H_6 were chosen to be the zero-point reference for the relative energy of every species on the same chart.

On the reactant side in Figure 2(a), there are separate reactants ($Ir_8 + C_2H_6$) and reactant complexes ($Ir_8{---}C_2H_6$), which leads to two different definitions of the energy barrier:

$$\text{True energy barrier} = E(TS) - E(Ir_8{---}C_2H_6)$$

$$\text{Apparent energy barrier} = E(TS) - E(Ir_8) - E(C_2H_6)$$

True energy barriers are always positive, whereas the apparent energy barrier can be zero or even negative when the attraction between Ir_8 and C_2H_6 is equal to or greater than the true energy barrier, which is indeed the case for all six reaction paths with M < 13. However, the reaction path in the 13-et state is considered to be the lowest-energy-barrier path despite its 65 kJ/mol apparent energy barrier; this is because ~80 kJ/mol or more energy (and electron spin flip) is necessary to excite the 13-et global minimum to the 11-et state or any other spin states.

For practical purposes, the catalytic activity of an Ir_n cluster is quantized in the following manner. For each reaction path in a specific spin state, its highest-energy structure (which is not necessarily the transition state) is considered to be the energy bottleneck of that path; and the

lowest-energy bottleneck among all reaction paths is considered to be the lowest-energy barrier for the $Ir_n + C_2H_6 \rightarrow H{-}Ir_n{-}C_2H_5$ reaction. The reaction path with the lowest energy barrier was plotted with thick solid lines, whereas all other reaction paths were plotted with thin dashed lines (Figure 2). Suppression of electron spin is observed as the Ir cluster size increases. For Ir_8, the reaction path with the lowest energy barrier is in the 13-et electronic state. For the corner and edge sites of Ir_{12}, the reaction paths with the lowest energy barrier are in the septet state and quintet state, respectively. For the corner, edge, and face-center sites of Ir_{18}, the reaction paths with the lowest energy barrier are all in the triplet state.

In the cuboid structure of Ir_{12}, Ir atoms may occupy two different sites: the corner site or edge site. Figures 2(b) and 2(c) illustrate the $Ir_{12} + C_2H_6 \rightarrow H{-}Ir_{12}{-}C_2H_5$ reaction paths at these two different sites. In order to make direct comparisons of the energy profiles at these two catalytic sites, the vertical axes of relative energy in Figures 2(b) and 2(c) have the same maximum and minimum values. The relative energies of the reactant complexes are virtually the same before Ir atom insertion into a C–H bond. However, the relative energies of the transition states are generally lower at the corner site than at the edge site. The lowest-energy barrier of the corner site is 21 kJ/mol in the septet state, whereas that of the edge site is 27 kJ/mol in the quintet state. The relative energies of the *products* of the corner site reactions are also lower than those of the edge site. This conspicuous site effect can be explained with the different coordination number of the inserting Ir atom: the corner Ir atom is more severely under-coordinated and thus more likely to accept the C-H σ bond electrons, forming Ir–C and Ir–H bonds. Electron flow from ethane to Ir_{12} is evidenced by both the Mulliken charge analysis and the frontier molecular orbital energy analysis. For example, Mulliken charge on a corner atom of an $^7Ir_{12}$ cluster changes from –0.07 to –0.21 when this corner atom inserts into a C–H bond in the

septet TS. The negative LUMO energy of $^{7}Ir_{12}$ (–0.16 Hartree) also indicates that the direction of the electron flow is from ethane to $^{7}Ir_{12}$. The site effect can also be explained by visualizing the shapes of the lowest unoccupied molecular orbitals (LUMO) of the Ir_{12} cluster in Figure 3(a): the LUMO lobes are more diffuse on the corner sites, and thus the corner Ir atoms accept the C–H σ bonding electrons more easily than the edge Ir atoms. This is also the case for the Ir_{18} cuboid, although Ir_{18} has a third type of site, the face-center sites, which are less reactive than both the corner and edge sites.

Figures 2(d–f) illustrate the reaction paths of Ir_{18} inserting into a C–H bond at three different sites: corner (2d), edge (2e), and face-center (2f) sites. The vertical axes of the relative energies of Figures 2(d–f) have the same maximum and minimum values. Similarly, electron flows from ethane to the inserting Ir_{18} cluster in these reactions. For example, Mulliken charge on a corner atom of an $^{3}Ir_{18}$ cluster changes from –0.09 to –0.25 when this corner atom inserts into a C–H bond in the triplet TS. The negative LUMO energy of $^{3}Ir_{18}$ (–0.16 Hartree) also indicates that the direction of the electron flow is from ethane to $^{3}Ir_{18}$. Clearly, the corner site insertion is favored both kinetically (lower TS energy) and thermodynamically (lower product energy) than the edge site. The face-center site has the lowest catalytic activity. The site effect can again be explained using the coordination number of the inserting Ir atom: the coordinate numbers of the corner, edge, and face-center atoms are 3, 4, and 5, respectively; and Ir atoms with lower coordination numbers tend to more readily insert into a C–H bond. Moreover, Figure 3(b) shows that the LUMOs of $^{3}Ir_{18}$ also have more diffuse lobes at the corners than at the edge and face-center sites. Figures 3(c) and 3(d) show a clear trend that the relative energy of the transition state of the corner site reaction is lower than those at the edge and face-center sites. The relative energies of the products exhibit the same trend in Figures 3(e) and 3(f). The corner-

site $Ir_{12} + C_2H_6 \rightarrow H{-}Ir_{12}{-}C_2H_5$ reaction releases as much as 100 kJ/mol heat, significantly more than that of the edge site; the corner-site $Ir_{18} + C_2H_6 \rightarrow H{-}Ir_{18}{-}C_2H_5$ reaction releases ~80 kJ/mol heat, also significantly more than those of the edge and face-center sites.

The enthalpy and Gibbs energy of activation of the $Ir_n + C_2H_6 \rightarrow H{-}Ir_n{-}C_2H_5$ reaction were also calculated. Figure 4(a) shows that the temperature dependence of the enthalpy of activation is negligible (~ 1 kJ/mol or less) from 0 K to 298 K. Figure 4(a) also clearly shows that the clusters' enthalpy of activation strongly depends on the cluster size and the catalytic site: Ir_{12} and Ir_{18} have a much stronger catalytic activity than Ir_8, and the corner-site Ir atoms exhibit stronger catalytic activity than the edge and face-center sites. Figure 4(b) shows that the Gibbs energy of activation is generally greater than the enthalpy of activation, due to the significant entropy decrease in the transition state structure compared to the much looser reactant structures. The entropy of activation ($\Delta S^{\neq}$) ranges approximately between –100 and –130 J/(mol K) relative to separated $Ir_n + C_2H_6$ reactants, resulting in a *ca.* 30−40 kJ/mol difference between the enthalpy and the Gibbs energy of activation at room temperature, given $\Delta G^{\neq} = \Delta H^{\neq} - T\Delta S^{\neq}$. For example, the lowest possible $\Delta H^{\neq}$ and $\Delta G^{\neq}$of $Ir_{18} + C_2H_6 \rightarrow H{-}Ir_{18}{-}C_2H_5$ are 3 kJ/mol and 31 kJ/mol, respectively, in the triplet electronic state. The extraordinarily small enthalpy of activation (3 kJ/mol) results from the significant enthalpy decrease (–54 kJ/mol) in the formation of the $^3Ir_{18}{---}C_2H_6$ complex. However, it is seemingly surprising that the enthalpy bottleneck (21 kJ/mol) and the Gibbs energy bottleneck (25 kJ/mol) for the $Ir_{12} + C_2H_6 \rightarrow H{-}Ir_{12}{-}C_2H_5$ reaction differ by merely 4 kJ/mol in the septet electronic state. This is because the *apparent* energy barrier of this reaction is –46 kJ/mol: the TS has significantly lower energy than the separated reactants. Consequently, the relative enthalpy or Gibbs energy of the separated reactants ($^7Ir_{12} + C_2H_6$), instead of the TS, are the bottleneck of the $Ir_{12} + C_2H_6 \rightarrow H{-}Ir_{12}{-}C_2H_5$ reaction paths.

Because the entropy of $^{7}Ir_{12}$ is 13 J/(mol K) smaller than that of the $^{11}Ir_{12}$ global minimum, the enthalpy and Gibbs energy bottlenecks for the $Ir_{12} + C_2H_6 \rightarrow H{-}Ir_{12}{-}C_2H_5$ reaction paths differ by only 13 J/(mol K) × 298 K ≈ 4 kJ/mol at room temperature. The above entropy analysis shows why ethane H-elimination at the Ir_{18} corner site has the lowest enthalpy of activation, whereas the reaction at the Ir_{12} corner site has the lowest Gibbs energy of activation at room temperature.

The product of the first H-elimination reaction, $H{-}Ir_n{-}C_2H_5$, lies ~80 kJ/mol (Ir_{18} corner site) or ~100 kJ/mol (Ir_{12} corner site) below the separated reactants. This substantial energy decrease suggests that the first hydrogen elimination is very likely the rate-limiting step of the ethane-to-ethene conversion, because the heat released from the first H-elimination may help overcome the energy barrier of the second H-elimination step, described next.

3.3 Second hydrogen elimination: $H{-}Ir_n{-}C_2H_5 \rightarrow (H)_2{-}Ir_n{-}C_2H_4$

After an Ir_n cluster inserts into a C–H bond of ethane, $H{-}Ir_n{-}C_2H_5$ is formed and may then undergo two different types of reactions: i) hydrogen migration on the Ir cluster surface, and ii) a second hydrogen-elimination that results in ethene. The energy barrier of the hydrogen migration has a small 10–30 kJ/mol energy barrier, and is thermodynamically favored in the direction of leaving the $Ir{-}C_2H_5$ site. Therefore, it is assumed that the first eliminated H migrates to a different position before the second H is removed from ethane. Eliminating a second H atom from ethane, $H{-}Ir_n{-}C_2H_5 \rightarrow (H)_2{-}Ir_n{-}C_2H_4$, has a larger energy barrier than the first H-elimination. This is because once an Ir atom bonds to C_2H_5, its previously empty d orbitals are occupied by electrons that originate from ethane, and the Ir atom also becomes more negatively charged. Therefore, the Ir atom bonded to C_2H_5 is less likely to attract additional C–H σ bonding electrons. On the other hand, there are two factors that favor the second H-elimination over the

first one: i) the second H-elimination results in the formation of a C−C partial π bond, suggested by the shortened C−C bond distance both in the transition state (R_{C-C} = 1.44 Å) and in the product (R_{C-C} = 1.41 Å) in comparison with that in the reactant (R_{C-C} = 1.53 Å); formation of the partial π bond stabilizes the TS and the product; and ii) overlap between the partial π bond and the d orbitals of the Ir atom provides additional stabilization via electron delocalization. Overall, the true energy barrier of the second H-elimination is slightly greater than the first barrier. The enthalpy of activation of $H{-}Ir_{12}{-}C_2H_5 \rightarrow (H)_2{-}Ir_{12}{-}C_2H_4$ is 74, 77, 83, and 72 kJ/mol in the spin states of M = 1, 3, 5, 7 (Figure 5), respectively. To rule out the impact of the first eliminated H atom on the second H-elimination step, we also studied the $Ir_{12}{-}C_2H_5 \rightarrow H{-}Ir_{12}{-}C_2H_4$ reaction. The enthalpy of activation of this reaction is 80, 75, or 84 kJ/mol in the doublet, quartet, or sextet spin states, respectively; virtually the same as the energy barriers of the $H{-}Ir_{12}{-}C_2H_5 \rightarrow (H)_2{-}Ir_{12}{-}C_2H_4$ reactions, with one additional H atom bonded to the Ir cluster surface.

The enthalpy profiles of the two H-elimination steps of $Ir_{12}{-}C_2H_6 \rightarrow H{-}Ir_{12}{-}C_2H_5 \rightarrow (H)_2{-}Ir_{12}{-}C_2H_4$ are illustrated in Figure 5. TS1 and TS2 are the transition states of the first and second H-elimination steps, respectively. TS' denotes the transition state(s) for the hydrogen migration on the Ir cluster surface. H-migration from $H{-}Ir_{12}{-}C_2H_5$ (A) to $H{-}Ir_{12}{-}C_2H_5$ (B) is thermodynamically favored, and has an estimated energy barrier of less than 30 kJ/mol.

H-migration on the Ir_{18} cluster surface and the second H-elimination of ethane catalyzed by Ir_{18} were also calculated in various spin states. Similarly, H-migration, with a smaller than 30 kJ/mol energy barrier, is expected to occur and release heat before the second H-elimination. Although the second H-elimination catalyzed by Ir_{18} has a slightly higher energy barrier (~90 kJ/mol) than the Ir_{12} case (~80 kJ/mol), energy released from the first H-elimination and from the

H-migration is sufficient to overcome this energy barrier. We next discuss oxygen adsorption effects on Ir cluster-catalyzed ethane dehydrogenation.

3.4 Effect of oxygen adsorbed on the Ir_n cluster surface

In an oxygen-rich environment, oxygen molecules may be adsorbed on the Ir cluster surface and decompose. The activation energy of O_2 dissociation on the Ir (100) or (111) surface is calculated to be ~25 kJ/mol or ~6 kJ/mol using the nudged elastic band (NEB) method.[40,41] We performed similar constrained geometry optimization calculations for selected O_2-Ir_{18} structures at various fixed O-O distances, allowing all other coordinates to fully relax. O_2 adsorption and dissociation on an Ir_{18} cluster surface are exothermic and virtually barrier-less in both triplet and quintet electronic states. We then calculated the H-elimination reaction path catalyzed by Ir_{18} clusters bonded to two O atoms for two different scenarios: i) adsorbed oxygen atoms are singly bonded to each other, denoted by O_2-Ir_{18}; and ii) adsorbed oxygen atoms are no longer bonded to each other, denoted by $(O)_2$-Ir_{18}. For each scenario we calculated the reaction path in both the triplet and quintet spin states. Figure 6 shows that O_2–Ir_{18} exhibits virtually the same catalytic activity as Ir_{18}, whereas $(O)_2$-Ir_{18} has slightly lower catalytic activity with an ~13 kJ/mol higher energy barrier than a free Ir_{18} cluster.

3.5 Propane vs ethane: oxidative dehydrogenation catalyzed by Ir_n

Since propane-to-propene conversion is also an important industrial process, and is similar to ethane-to-ethene conversion, we studied the first H-elimination in propane, $Ir_n{-}C_3H_8 \rightarrow H{-}Ir_n{-}C_3H_7$ for Ir_{18}, in the triplet and quintet states. Figure 7 shows that the H-elimination of propane is slightly more favored than that of ethane, from both kinetic and thermodynamic standpoints. This is due to further stabilization of the reactant complex, transition state, and

product by the additional methyl group in propane. The first H-elimination reaction is virtually barrier-free and thus is primarily diffusion-controlled. Thus, Ir_{12} and Ir_{18} should also be effective catalysts towards propane-to-propene conversion.

4. Conclusions

The B3LYP-D3BJ method was used to model the Ir catalyzed dehydrogenation of ethane, a common industrial reaction. The first H-elimination step is the rate-limiting step; there is sufficient heat release to overcome the energy barrier of H-migration and the second H-elimination. Ir_{12} and Ir_{18} are both more effective catalysts than Ir_8. In particular, the corner sites of Ir_{12} and Ir_{18} cuboids are more reactive than the edge sites, whereas the face-center sites are the least reactive. The different catalytic activities of the three different sites is due to the diffusivity of the LUMO of the Ir clusters at the corner site, which facilitates acceptance of the C–H σ bonding electrons. In an oxygen-rich environment, oxygen absorption on the Ir cluster surface slightly increases the energy barrier for the H-elimination, but the reaction between the oxygen and hydrogen atoms on the Ir cluster surface renders ethane dehydrogenation thermodynamically favorable. We also performed calculations for H-elimination of propane, which was more favorable (from both kinetic and thermodynamic standpoints) than that of ethane. In summary, in comparison with the Ir_4 and Ir_6 clusters studied previously,[2,3,5] larger Ir_{12} and Ir_{18} clusters also have strong catalytic activity towards dehydrogenation of small alkanes, and should bind to supporting surfaces more strongly. The thermodynamic stability of the Ir_{12} and Ir_{18} cuboids makes the production of these clusters feasible using chemical or physical vapor deposition techniques. Most importantly, this paper illustrates a strategy for transition metal nanocatalyst immobilization on supporting surfaces that hinders deleterious migration and coalescence.

Acknowledgments: Y. Ge thanks the Central Washington University (CWU) Faculty Research Program and School of Graduate Studies and Research for financial support of this work. Y. Ge also thanks the CWU Information Services for granting access to their high-performance computers, and particularly Bill Glessner for technical assistance. The authors are indebted to M. Scott Long for critically proofreading the manuscript.

References

(1) Sattler, J. J. H. B.; Ruiz-Martinez, J.; Santillan-Jimenez, E.; Weckhuysen, B. M. Catalytic Dehydrogenation of Light Alkanes on Metals and Metal Oxides. *Chem. Rev.* **2014**, *114*, 10613–10653.

(2) Xu, Z.; Xiao, F. S.; Purnell, S. K.; Alexeev, O.; S., K.; Deutsch, S. E.; Gates, B. C. Size-Dependent Catalytic Activity of Supported Metal Clusters. *Nature* **1994**, *372*, 346–348.

(3) Argo, A. M.; Odzak, J. F.; Lai, F. S.; Gates, B. C. Observation of Ligand Effects during Alkene Hydrogenation Catalysed by Supported Metal Clusters. *Nature* **2002**, *415*, 623–626.

(4) Uzun, A.; Dixon, D. A.; Gates, B. C. Prototype Supported Metal Cluster Catalysts: Ir_4 and Ir_6. *ChemCatChem* **2011**, *3*, 95–107.

(5) Argo, A. M.; Odzak, J. F.; Gates, B. C. Role of Cluster Size in Catalysis: Spectroscopic Investigation of γ-Al_2O_3-Supported Ir_4 and Ir_6 during Ethene Hydrogenation. *J. Am. Chem. Soc.* **2003**, *125*, 7107–7115.

(6) Ferguson, G. A.; Mehmood, F.; Rankin, R. B.; Greeley, J. P.; Vajda, S.; Curtiss, L. A. Exploring Computational Design of Size-Specific Subnanometer Clusters Catalysts. *Top. Catal.* **2012**, *55*, 353–365.

(7) Vajda, S.; Pellin, M. J.; Greeley, J. P.; Marshall, C. L.; Curtiss, L. A.; Ballentine, G. A.; Elam, J. W.; Catillon-Mucherie, S.; Redfern, P. C.; Mehmood, F.; et al. Subnanometre Platinum Clusters as Highly Active and Selective Catalysts for the Oxidative Dehydrogenation of Propane. *Nat. Mater.* **2009**, *8*, 213–216.

(8) Han, C. W.; Iddir, H.; Uzun, A.; Curtiss, L. A.; Browning, N. D.; Gates, B. C.; Ortalan, V. Migration of Single Iridium Atoms and Tri-Iridium Clusters on MgO Surfaces: Aberration-Corrected STEM Imaging and Ab Initio Calculations. *J. Phys. Chem. Lett.* **2015**, *6*, 4675–4679.

(9) Mei, D. H.; Kwak, J. H.; Hu, J. Z.; Cho, S. J.; Szanyi, J.; Allard, L. F.; Peden, C. H. F. Unique Role of Anchoring Penta-Coordinated Al3+ Sites in the Sintering of γ-Al_2O_3-Supported Pt Catalysts. *J. Phys. Chem. Lett.* **2010**, *1*, 2688–2691.

(10) Davis, J. B. A.; Shayeghi, A.; Horswell, S. L.; Johnston, R. L. The Birmingham Parallel Genetic Algorithm and Its Application to the Direct DFT Global Optimisation of Ir_N (N = 10-20) Clusters. *Nanoscale* **2015**, *7*, 14032–14038.

(11) Chen, M.; Dixon, D. A. Low-Lying Electronic States of Ir_n Clusters with n=2-8 Predicted at the DFT, CASSCF, and CCSD(T) Levels. *J. Phys. Chem. A* **2013**, *117*, 3676–3688.

(12) Li, S.; Li, H.; Liu, J.; Xue, X.; Tian, Y.; He, H.; Jia, Y. Structural and Electronic Properties of Ru_n Clusters (n=2-14) Studied by First-Principles Calculations. *Phys. Rev. B* **2007**, *76*, 45410.

(13) Afeefy, H. Y.; Liebman, J. F.; Stein, S. E. Neutral Thermochemical Data. In NIST Chemistry WebBook; Linstrom, P. J., Mallard, W. G., Eds; NIST Standard Reference Database Number 69; National Institute of Standards and Technology: Gaithersburg, MD, http://webbook.nist.gov, (retrieved 9/28/2016).

(14) Becke, A. D. Density-Functional Thermochemistry. III. The Role of Exact Exchange. *J. Chem. Phys.* **1993**, *98*, 5648–5652.

(15) Lee, C.; Yang, W.; Parr, R. G. Development of the Colle-Salvetti Correlation-Energy Formula into a Functional of the Electron Density. *Phys. Rev. B* **1988**, *37*, 785–789.

(16) Stephens, P. J.; Devlin, F. J.; Chabalowski, C. F.; Frisch, M. J. Ab Initio Calculation of Vibrational Absorption and Circular Dichroism Spectra Using Density Functional Force Fields. *J. Phys. Chem.* **1994**, *98*, 11623–11627.

(17) Grimme, S.; Ehrlich, S.; Goerigk, L. Effect of the Damping Function in Dispersion Corrected Density Functional Theory. *J. Comput. Chem.* **2011**, *32*, 1456–1465.

(18) Hay, P. J.; Wadt, W. R. Ab Initio Effective Core Potentials for Molecular Calculations. Potentials for K to Au Including the Outermost Core Orbitals. *J. Chem. Phys.* **1985**, *82*, 299–310.

(19) Ehlers, A. W.; Bohme, M.; Dapprich, S.; Gobbi, A.; Hollwarth, A.; Jonas, V.; Kohler, K. F.; Stegmann, R.; Veldkamp, A.; Frenking, G. A Set of F-Polarization Functions for Pseudo-Potential Basis Sets of the Transition Metals Sc–Cu, Y–Ag and La–Au. *Chem. Phys. Lett.* **1993**, *208*, 111–114.

(20) Hehre, W. J.; Ditchfield, R.; Pople, J. A. Self-Consistent Molecular-Orbital methods.12. Further Extensions of Gaussian-Type Basis Sets for Use in Molecular-Orbital Studies of Organic-Molecules. *J. Chem. Phys.* **1972**, *56*, 2257–2261.

(21) Hariharan, P. C.; Pople, J. A. The Influence of Polarization Functions on Molecular Orbital Hydrogenation Energies. *Theo. Chim. Acta* **1973**, *28*, 213–222.

(22) Roy, L. E.; Hay, P. J.; Martin, R. L. Revised Basis Sets for the LANL Effective Core Potentials. *J. Chem. Theory Comput.* **2008**, *4*, 1029–1031.

(23) Krishnan, R.; Binkley, J. S.; Seeger, R.; Pople, J. A. Self-Consistent Molecular Orbital Methods. XX. A Basis Set for Correlated Wave Functions. *J. Chem. Phys.* **1980**, *72*, 650–654.

(24) Schmidt, M. W.; Baldridge, K. K.; Boatz, J. A.; Elbert, S. T.; Gordon, M. S.; Jensen, J. H.; Koseki, S.; Matsunaga, N.; Nguyen, K. A.; Su, S. J.; et al. General Atomic and Molecular Electronic-Structure System. *J. Comput. Chem.* **1993**, *14*, 1347–1363.

(25) Gordon, M. S.; Schmidt, M. W. Advances in Electronic Structure Theory: GAMESS a Decade Later. In *Theory and Applications of Computational Chemistry, Ch. 41*; Dykstra, C. E., Frenking, G., Kim, K. S., Scuseria, G. E., Eds.; Elsevier, 2005.

(26) Frisch, M. J.; Trucks, G. W.; Schlegel, H. B.; Scuseria, G. E.; Robb, M. A.; Cheeseman, J. R.; Scalmani, G.; Barone, V.; Mennucci, B.; Petersson, G. A., et al. *Gaussian 09*, Revision D.1; Gaussian, Inc.: Wallingford, CT, 2009.

(27) Grimme, S. Semiempirical Hybrid Density Functional with Perturbative Second-Order Correlation. *J. Chem. Phys.* **2006**, *124*, 34108.

(28) Adamo, C.; Barone, V. Toward Reliable Density Functional Methods without Adjustable Parameters: The PBE0 Model. *J. Chem. Phys.* **1999**, *110*, 6158–6169.

(29) Becke, A. D. Density-Functional Exchange-Energy Approximation with Correct Asymptotic Behavior. *Phys. Rev. A* **1988**, *38*, 3098–3100.

(30) Perdew, J. P.; Burke, K.; Ernzerhof, M. Generalized Gradient Approximation Made Simple. *Phys. Rev. Lett.* **1996**, *77*, 3865–3868.

(31) Hohenberg, P.; Kohn, W. Inhomogeneous Electron Gas. *Phys. Rev.* **1964**, *136*, B864–B871.

(32) Kohn, W.; Sham, L. J. Self-Consistent Equations Including Exchange and Correlation Effects. *Phys. Rev.* **1965**, *140*, A1133–A1138.

(33) Slater, J. C. *The Self-Consistent Field for Molecular and Solids, Quantum Theory of Molecular and Solids Volume 4. (Pure & Applied Physics)*; McGraw-Hill: New York, 1974.

(34) Vosko, S. H.; Wilk, L.; Nusair, M. Accurate Spin-Dependent Electron Liquid Correlation Energies for Local Spin Density Calculations: A Critical Analysis. *Can. J. Phys.* **1980**, *58*, 1200–1211.

(35) Piecuch, P.; Kucharski, S. A.; Kowalski, K.; Musial, M. Efficient Computer Implementation of the Renormalized Coupled-Cluster Methods: The R-CCSD[T], R-CCSD(T), CR-CCSD[T], and CR-CCSD(T) Approaches. *Comput. Phys. Commun.* **2002**, *149*, 71–96.

(36) Piecuch, P.; Wloch, M. Renormalized Coupled-Cluster Methods Exploiting Left Eigenstates of the Similarity-Transformed Hamiltonian. *J. Chem. Phys.* **2005**, *123*, 224105.

(37) Piecuch, P.; Wloch, M.; Gour, J. R.; Kinal, A. Single-Reference, Size-Extensive, Non-Iterative Coupled-Cluster Approaches to Bond Breaking and Biradicals. *Chem. Phys. Lett.* **2006**, *418*, 467–474.

(38) Wloch, M.; Gour, J. R.; Piecuch, P. Extension of the Renormalized Coupled-Cluster Methods Exploiting Left Eigenstates of the Similarity-Transformed Hamiltonian to Open-Shell Systems: A Benchmark Study. *J. Phys. Chem. A* **2007**, *111*, 11359–11382.

(39) Shore, T. C.; Mith, D.; DePrekel, D.; McNall, S.; Ge, Y. A B3LYP Study on the C–H

Activation in Propane by Neutral and +1 Charged Low-Energy Platinum Clusters with 2–6 Atoms. *React. Kinet. Mech. Catal.* **2013**, *109*, 315–333.

(40) Erikat, I. A.; Hamad, B. A.; Khalifeh, J. M. A Density Functional Study on Adsorption and Dissociation of O_2 on Ir(100) Surface. *Chem. Phys.* **2011**, *385*, 35–40.

(41) Xu, Y.; Mavrikakis, M. Adsorption and Dissociation of O_2 on Ir(111). *J. Chem. Phys.* **2002**, *116*, 10846–10853.

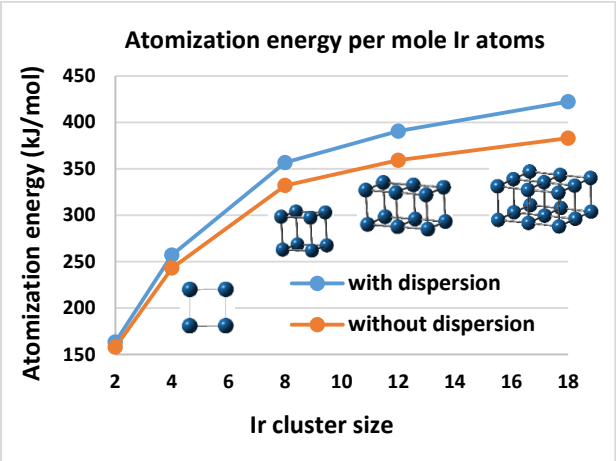

Figure 1. Atomization energy per atom of Ir_n clusters calculated using the B3LYP method: with D3BJ dispersion vs. without D3BJ dispersion.

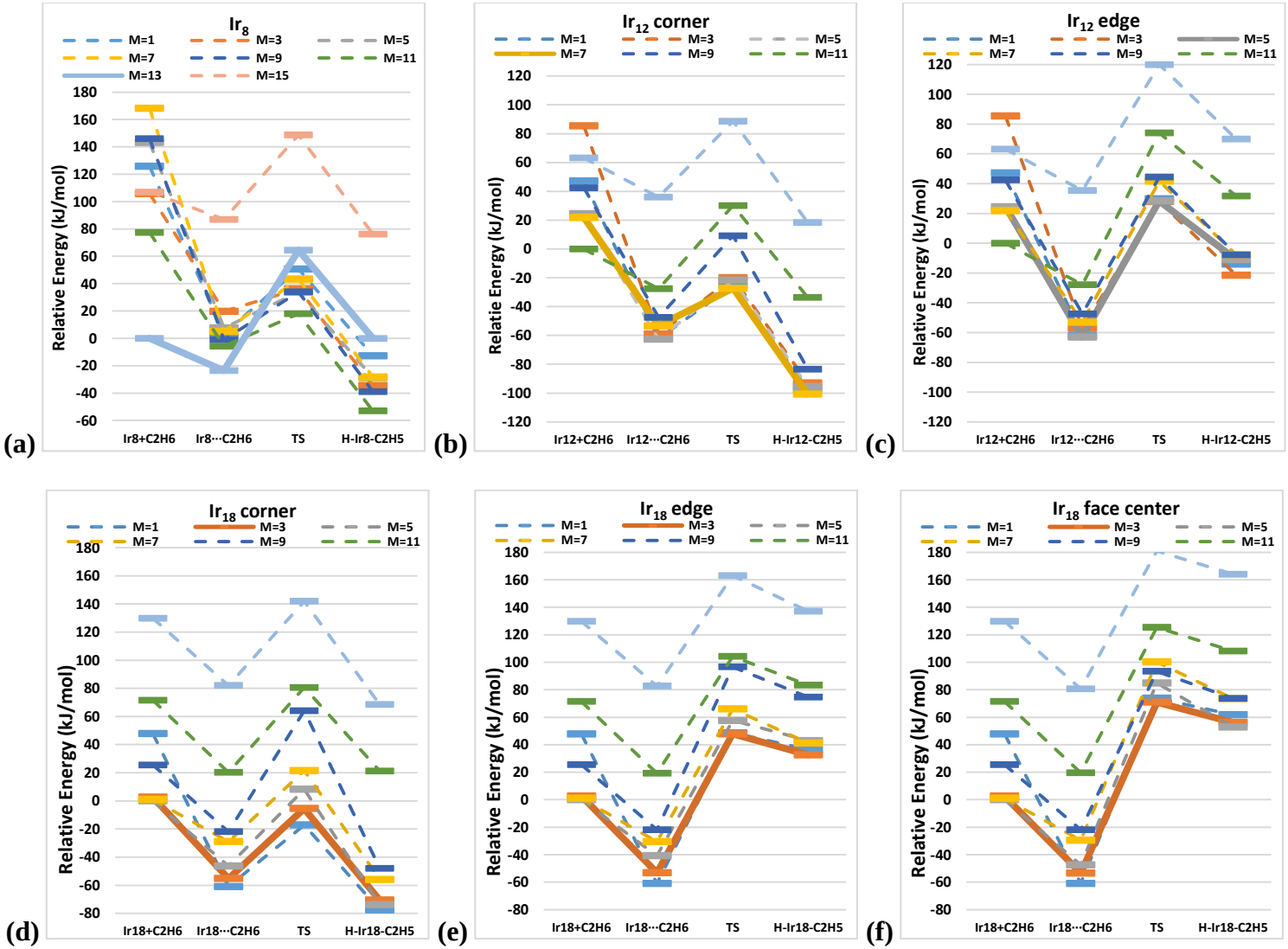

Figure 2. Relative energies (kJ/mol) of the $Ir_n + C_2H_6 \rightarrow H{-}Ir_n{-}C_2H_5$ reaction path: (a) Ir_8, (b–c) Ir_{12} corner and edge sites, (d–f) Ir_{18} corner, edge, and face-center sites. Zero-point vibrational energies are included.

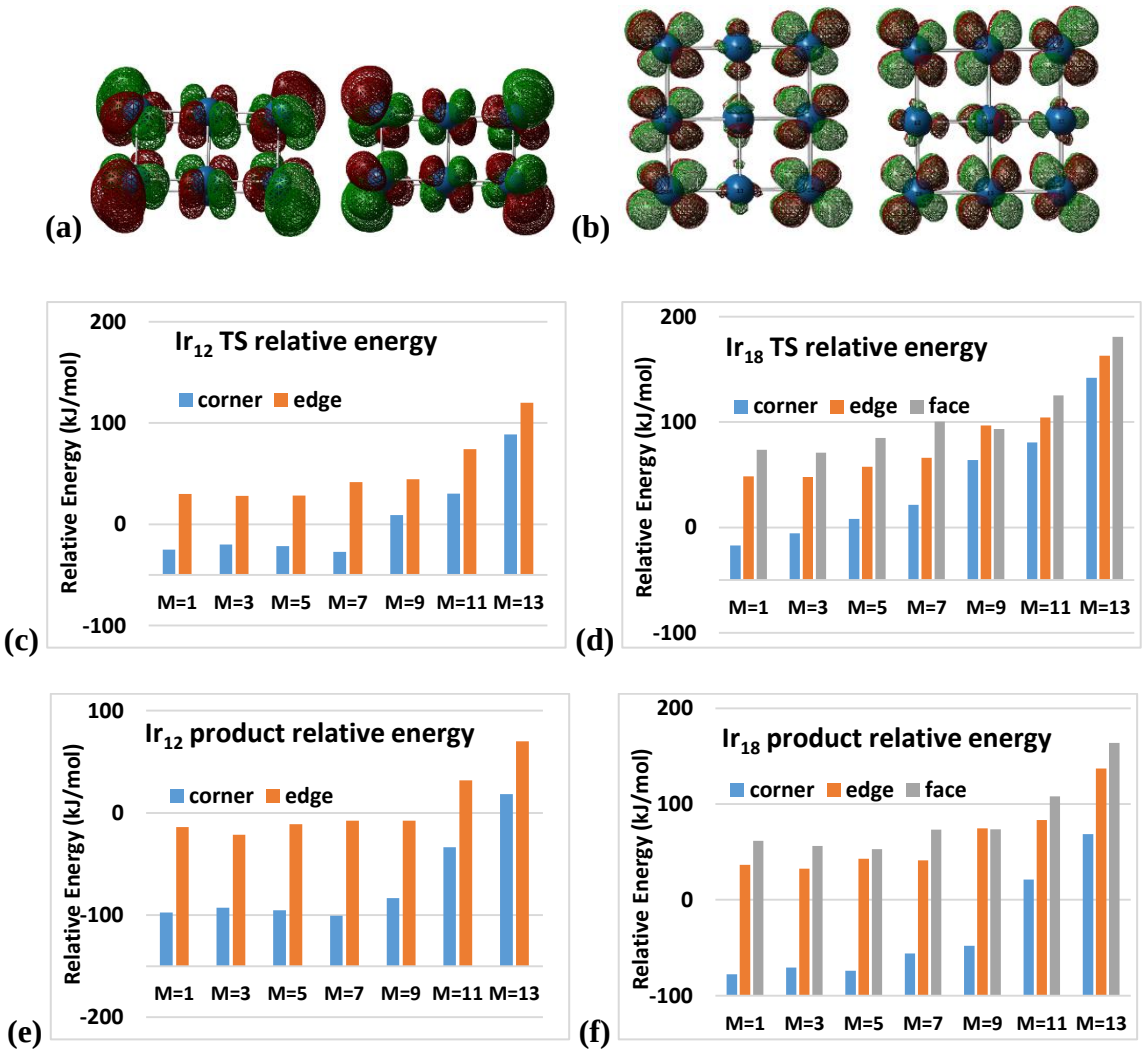

Figure 3. Top: (a) the two degenerate LUMOs of $^{5}Ir_{12}$ and (b) the two degenerate LUMOs of $^{3}Ir_{18}$. Middle: relative energies of transition states of (c) Ir_{12}- and (d) Ir_{18}-catalyzed H-elimination of ethane at the various sites. Bottom: relative energies of products of (e) Ir_{12} and (f) Ir_{18}-catalyzed H-elimination of ethane at the various sites.

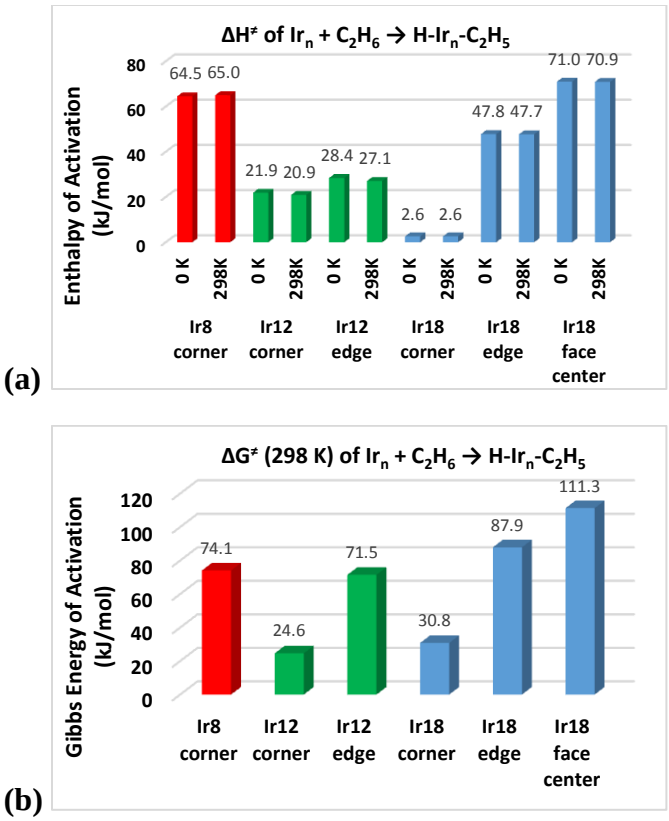

Figure 4. (a) Enthalpy of activation of the $Ir_n + C_2H_6 \rightarrow H\text{-}Ir_n\text{-}C_2H_5$ reaction (n = 8, 12, 18) on the corner, edge, and face-center sites at 0 K and 298 K. (b) Gibbs free energy of activation of the same reaction at 298 K.

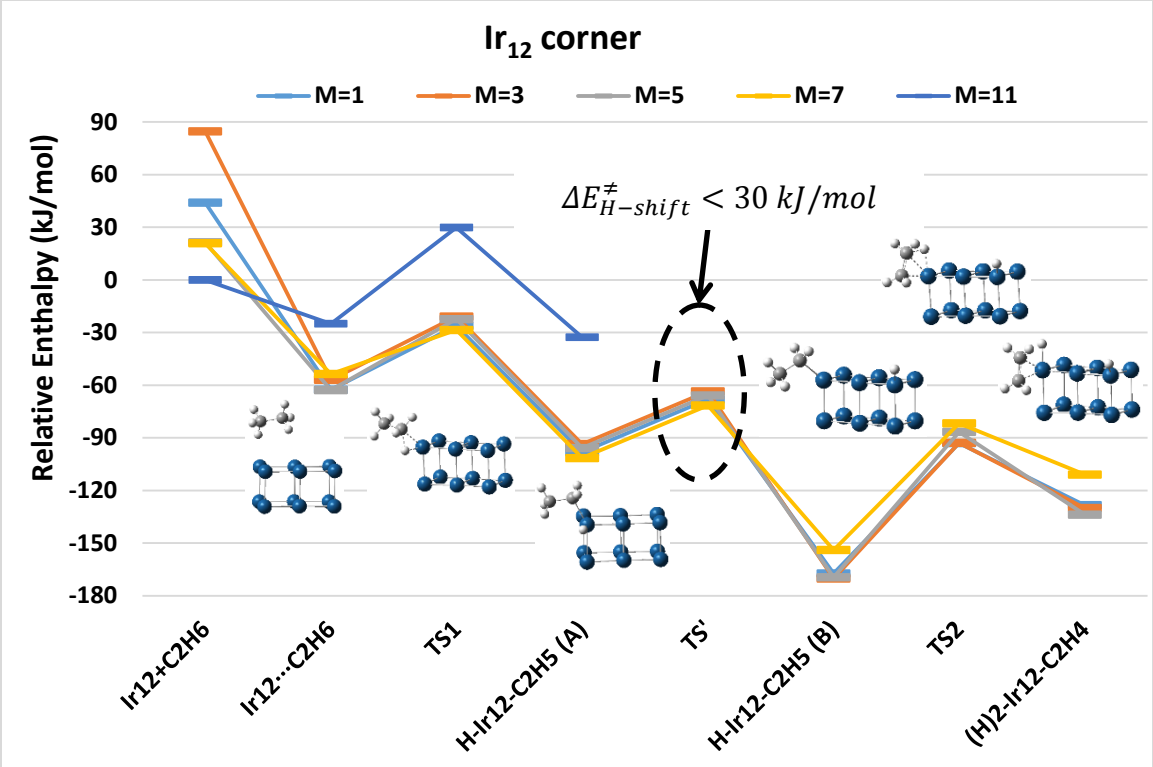

Figure 5. Relative enthalpies of the $Ir_{12} + C_2H_6 \rightarrow H{-}Ir_{12}{-}C_2H_5 \rightarrow (H)_2{-}Ir_{12}{-}C_2H_4$ reaction path in the spin state of M = 1, 3, 5, and 7 at 298 K. H-Ir_{12}-C_2H_5 (A) and H-Ir_{12}-C_2H_5 (B) differ in the position of the first eliminated H atom. The first half of the M = 11 reaction path is also shown, solely to provide a zero-point reference of relative enthalpies.

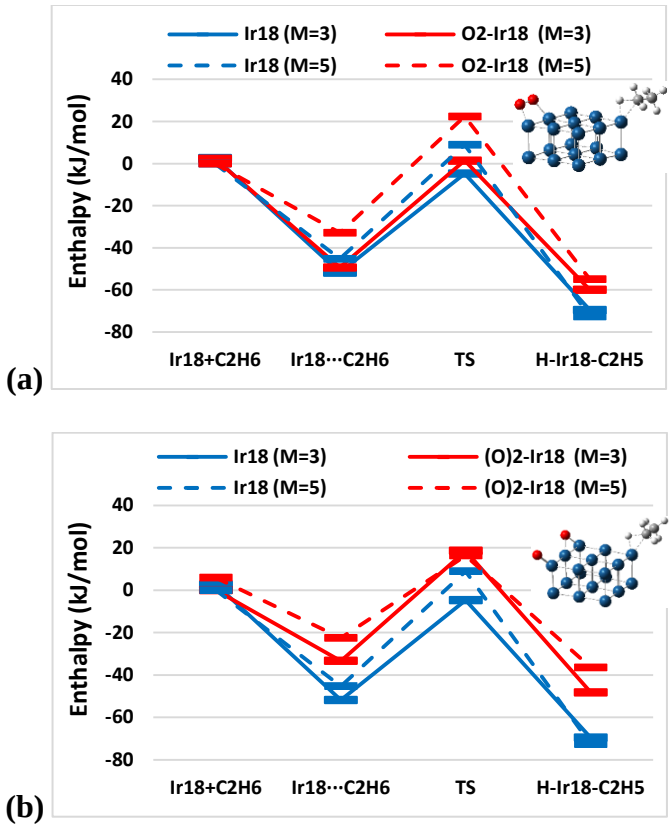

Figure 6. Relative enthalpy of Ir_{18} + C_2H_6 → H-Ir_{18}-C_2H_5 reaction at 298 K, without vs with absorbed oxygen on the Ir cluster surface. (a) Ir_{18} vs O_2-Ir_{18} with a single bond between the O atoms. (b) Ir_{18} vs $(O)_2$-Ir_{18} with the two oxygen atoms separated. Transition state structures are presented to illustrate the positions of the O atoms.

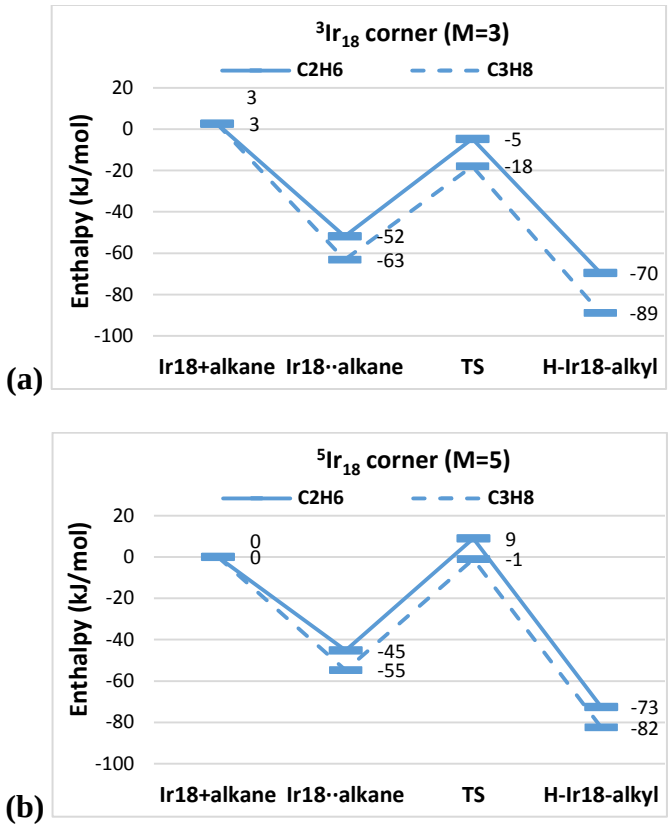

Figure 7. Relative enthalpy of the $Ir_{18} + C_mH_{2m+2} \rightarrow H\text{-}Ir_{18}\text{-}C_mH_{2m+1}$ reaction (m = 2, 3) at 298 K in (a) triplet and (b) quintet spin states.

TOC Graphic

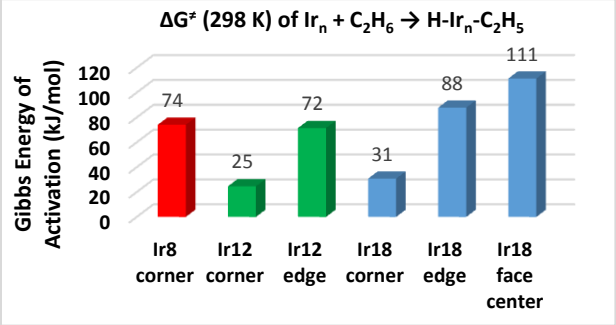
ΔG≠ (298 K) of Irn + C2H6 → H-Irn-C2H5
Gibbs Energy of Activation (kJ/mol)
120
100
80
60
40
20
0
74
25
72
31
88
111
Ir8 corner
Ir12 corner
Ir12 edge
Ir18 corner
Ir18 edge
Ir18 face center